Reaction Chemistry & Engineering

PAPER

Check for updates

Insights into the roles of water on the aqueous phase reforming of glycerol†

Tianjun Xie, [iD] Cameron J. Bodenschatz [iD] and Rachel B. Getman [iD] *

Aqueous phase reforming (APR) of sugar alcohol molecules derived from biomass, *e.g.*, $C_xH_{(2x+2)}O_x$ (aq) + $xH_2O \rightarrow xCO_2$ (g) + (2x + 1)H_2 (g), creates hydrogen gas sustainably, making it an important component of future bio-refineries; however, problems with the cost, activity, and selectivity of present precious metal based catalysts impede its broader adoption. Ideally, new catalysts would be designed to optimize activity and selectivity; however, a comprehensive understanding of the APR mechanism is lacking. This is complicated by the fact that the primary biomass-derived sugar alcohols are large molecules (meaning that their reaction networks are large) and because of the presence of liquid water. Water influences catalytic phenomena in multiple ways, including altering the thermodynamics of catalytic surface species and participating in catalytic reactions. Understanding the mechanism of APR requires understanding these various effects; however, computational strategies based solely on density functional theory (DFT) are computationally prohibitive for such large and complicated reaction networks. In this work, we investigate the mechanism of APR reactions in the context of glycerol reforming. To calculate the reaction network, we combine DFT calculations, force-field molecular dynamics (MD) simulations, linear scaling relations (LSRs), transition state scaling (TSS) relationships, and data from the literature into a microkinetic model. The microkinetic model is run under vacuum and aqueous phases in order to learn about the roles of water molecules on the mechanism of glycerol APR. We identify four such roles: providing surface hydroxyl groups, which promote oxidation of surface CO formed in glycerol decomposition; promoting C–H scissions; promoting O–H scissions; and inhibiting the thermodynamics of decarbonylation of C3 intermediates.

Department of Chemical and Biomolecular Engineering, Clemson University, USA.
E-mail: rgetman@clemson.edu
† Electronic supplementary information (ESI) available. See DOI: 10.1039/c8re00267c

Rachel B. Getman is an Associate Professor of Chemical and Biomolecular Engineering at Clemson University and the first woman to be tenured and promoted in her department. Her research group uses quantum chemical calculations and Monte Carlo and molecular dynamics simulations to investigate molecular-level phenomena at fluid/solid interfaces. Dr. Getman earned dual BS degrees in Chemical Engineering and Business Administration from Michigan Technological University in 2004. She earned her PhD from the University of Notre Dame in 2009, where she worked with William Schneider. From 2009–2011, she was a Postdoctoral Research Fellow with Randall Snurr at Northwestern University.

Rachel B. Getman

1 Introduction

As the main byproduct of biodiesel production, glycerol ($C_3H_8O_3$) is produced in surplus. There is thus interest in finding ways to convert it to more valuable products. One method for converting glycerol is aqueous phase reforming (APR). In APR, glycerol and/or other polyols (glucose, sorbitol) are converted to H_2 (g) and CO_2 (g) over supported metal catalysts in aqueous conditions.[1–4] The process is run at relatively low temperatures (around 500 K) just above the saturation pressure of liquid water. APR thus provides a sustainable source of H_2 (g) and can be carried out at mild conditions. The H_2 that is produced could be used in a biorefinery, for example, supplying the H_2 (g) needed for hydrodeoxygenation of biomass derivatives such as phenol (*i.e.*, $C_6H_5OH + H_2 \rightarrow C_6H_6 + H_2O$).[5] However, to date, H_2 yields have been low. A goal within the catalyst research community is to solve this problem, which first requires improving our understanding of the APR catalytic mechanism. From a big-picture standpoint, the mechanism of APR involves three branches: dehydrogenation (R–H* + * → R* + H*, where * are catalyst sites), decarbonylation (R–CO* + * → R* + CO*), and water-gas shift (WGS; CO* + H_2O → * + CO_2 + H_2). However, elucidating the individual steps in the different branches is not

straightforward for multiple reasons, including the large sizes and complex structures of APR feed molecules (which result in large reaction networks and numerous possible catalytic intermediates) and the aqueous reaction conditions themselves.

Given their strength in providing insight about molecular level details, computational strategies have contributed to understanding the mechanism of APR. For example, DFT studies have shown that catalytic glycerol reforming follows the path α-carbon dehydrogenation → β-carbon dehydrogenation → hydroxyl group dehydrogenation → decarbonlyation.[6–12] Our group is particularly interested in how the water environment influences the catalysis. Water is known to influence catalysis in multiple ways, including altering the energies of catalytic species *via* hydrogen bonding and other interactions (*e.g.*, van der Waals effects),[13–28] influencing the dominant reaction pathway,[14,15,23–25,29–31] and participating in the catalytic chemistry (*e.g.*, by enabling proton transfer).[29,32] We have previously investigated how the energies of catalytic species that could be involved in APR are influenced by the aqueous phase environment.[33,34] In this work, we continue that investigation and additionally explore the roles of water on the mechanism of glycerol APR over a Pt(111) catalyst.

Specifically, we use a combination of density functional theory (DFT) calculations, force field molecular dynamics (MD) simulations, and microkinetic modeling to learn about the mechanism of glycerol APR under aqueous conditions. Building on the literature, we construct and employ linear correlations for estimating the energies of catalytic C3 species in order to reduce the computational cost associated with studying such a large reaction network. Specifically, we use linear scaling relationships (LSRs)[34–43] built in our prior work[34] to estimate the energies of catalytic reactant and product species. Further, we build transition state scaling (TSS) relationships[6,44–50] to estimate the energies of transition states involved in dehydrogenation, decarbonylation, and hydrogenolysis reactions (R–OH* + * → R* + OH*) involving C3 catalytic intermediates. To investigate the ability of H_2O to participate in the catalysis, we additionally simulate water-mediated dehydrogenation (R–H* + $nH_2O^* \rightarrow R^* + H_{(2n+1)}O_n^*$)

and hydrogenolysis steps (R–OH* + $H_{(2n+1)}O_n^* \rightarrow R^* + (n + 1)H_2O^*$). We combine all of our calculated energies with energies obtained from the literature[40,51–53] for reactions involving C2 and C1 intermediates as well as WGS reactions into a microkinetic model, which we use to probe the mechanism of glycerol APR. Our results indicate that H_2O molecules play at least four roles in the APR of glycerol: supplying OH* for the WGS reaction, promoting C–H bond scissions, promoting O–H bond scissions, and inhibiting decarbonylation of C3 species.

2 Computational details

We calculate energies for this manuscript in two ways: explicitly and using linear relationships. In explicit calculations,

catalytic species are modeled under structures of liquid water using a multi-timescale method that combines DFT calculations and molecular dynamics simulations. This method is discussed below and elaborated in the ESI† section S5.

2.1 Simulation supercell

Pt(111) surfaces were modeled using three-layer 4 Pt × 4 Pt orthogonal slabs (*i.e.*, with symmetries of $p\left(2\sqrt{2} \times 7/4\sqrt{2}\right)$ – R90°) in periodic supercells. The slabs were constructed by cleaving a (111) surface from the calculated structure of bulk Pt. Catalytic intermediates and transition states were optimized on the topmost Pt layers only, and only one catalytic intermediate or transition state was included per slab, yielding a total coverage of 1/16 monolayer (ML, where 1 ML = 1 catalytic intermediate or transition state per surface Pt atom). The orthogonal supercells had dimensions of $a = 11.22$ Å and $b = 9.72$ Å. A total of 36 H_2O molecules were added to the supercell in the space above the Pt(111) surfaces. It has been shown by López that rigidity in the liquid H_2O structure can influence reactivity.[54] To ensure that liquid H_2O is simulated at the correct density for the reaction conditions, *i.e.*, $T = 500$ K and $P = 50$ bar, the c dimension of the supercell was determined using MD simulations performed in the NPT ensemble. This procedure is elaborated upon in section S2 of the ESI† as well as in an upcoming publication from our group.[55] Briefly, after the H_2O molecules are added to the supercell, a 5 ns MD simulation is performed in the NPT ensemble at a target temperature and pressure of 500 K and 50 bar, which are maintained by the Nosé–Hoover thermostat and barostat. The first 2 ns of the NPT simulation are used for system equilibration and the remaining 3 ns are used to determine the average value of the c dimension. The value of the c dimension that yields the proper H_2O density for these supercells is 20.18 Å. The resulting liquid water density is 0.857 g cm^{-3}, which is similar to the density of saturated liquid water at 500 K as calculated with TIP4P/2005 (0.850 g cm^{-3} (ref. 56)) and as observed experimentally (0.844 g cm^{-3} (ref. 57) and 0.837 g cm^{-3} (ref. 58)).

2.2 Water configurations from molecular dynamics simulations

Molecular dynamics (MD) simulations were conducted using the large-scale atomic/molecular massively parallel simulator (LAMMPS).[59] Interactions of water molecules with catalytic intermediates and the Pt surface were calculated using Lennard Jones + Coulomb (LJ + C) potentials. LJ parameters for adsorbates, H_2O molecules, and Pt atoms were taken from the optimized potentials for liquid simulations (OPLS),[60] TIP4P/2005,[61] and INTERFACE force fields,[62] respectively. Cross terms for the LJ interactions were computed using Lorentz–Berthelot mixing rules.[63,64] Atomic partial charges used in the Coulomb potentials for the Pt atoms and adsorbates were calculated from density functional theory results using the density derived electrostatic and chemical

(DDEC) package.[65–70] All LJ + C parameters are tabulated in the ESI† section S3.

Configurations of liquid H_2O molecules around the catalytic species were generated in the NVT ensemble. The target temperature was set to 500 K, similar to the conditions employed experimentally.[71–74] The temperature was controlled by the Nosé–Hoover thermostat.[75] MD simulations were performed for 5 ns with 1 fs timesteps, where the first 2 ns were used for system equilibration and the final 3 ns were used for configurational sampling.

2.3 Energies of catalytic species from DFT

DFT calculations were performed using the Vienna *ab initio* simulation package (VASP),[76–79] which employs plane-wave basis sets and periodic boundary conditions. Projector augmented wave (PAW)[80,81] pseudopotentials were used to model the core electrons to an energy cutoff of 400 eV. Exchange and correlation of the valence electrons were captured with the Perdew–Burke–Ernzerhof (PBE)[82] form of the generalized gradient approximation (GGA). Gaussian smearing with a smearing factor of 0.1 eV was employed. The D2 correction[83] was applied to account for dispersion interactions. The choice of dispersion correction has been shown to influence the energies of adsorption on metal surfaces.[84–86] Calculations performed with and without the D2 method indicate that the D2 method influences the energies of surface reactions by 0.1 eV or less. These comparisons are made in section S1 of the ESI.† Automatically generated Monkhorst–Pack[87] Γ-centered 7 × 7 × 1 k-point meshes were applied to sample the first Brillouin zones. Electronic structure calculations were performed iteratively, and electronic structures were considered to be converged when the energy difference between subsequent iterations fell below 10^{-6} eV. Geometries of catalytic species were located using geometry relaxation calculations and were considered to be converged when the maximum force on all non-fixed atoms fell below 0.03 eV Å^{-1}. Transition states were identified using a combination of the climbing image-nudged elastic band (CI-NEB)[88,89] and dimer methods[90] and were also considered to be converged when the maximum force on all non-fixed atoms fell below 0.03 eV Å^{-1}. All transition state structures were confirmed by their vibrational frequencies. The final structures of all catalytic species calculated in this work are illustrated in ESI† section S6. Additionally, their coordinates have been uploaded to our group's GitHub page.[91] VASP INCAR settings are provided in the ESI† section S1.

2.4 Linear scaling and transition state scaling relationships

Since the reaction network for catalytic APR is rather large, we additionally estimated energies of catalytic species using linear correlations, as has been done by others working in this field.[92] Binding energies of C3 intermediates (reactant and product species) were estimated using an extended linear scaling relationship (LSR) based on the energies of their fragments,[35–43,93] as in our prior work.[34] In our prior work, we derived linear correlations to calculate the energies of intermediates with chemical formulas of CHy'O–CHy''O–CHy'''O as functions of the binding energies of their CHy'O, CHy''O, and CHy'''O fragments (the subscripts y', y'', and y''' denote different levels of saturation of the carbon atoms). Energies of transition states were estimated using transition state scaling (TSS) relationships,[6,44–50] which are linear functions of the energies of the product species (commonly referred to as final state (FS) species in the literature). In this work, we input both DFT calculated FS energies and FS energies that were calculated using LSRs to the TSS relationships. How we combined LSRs and TSS relationships is demonstrated in the ESI† section S4.

2.5 Reaction and activation energy calculations

Reaction energies for vacuum phase reactions E_{rxn}^{vac} were calculated using standard formulas. For example, the reaction energy for adsorbed glycerol $C_3H_8O_3^*$ dehydrogenation to $C_3H_7O_3^*$, *i.e.*, $C_3H_8O_3^* + * \rightarrow C_3H_7O_3^* + H^*$ (where * indicates a catalytic site and a *'ed species indicates a species adsorbed on a Pt(111) catalytic site) is

$$E_{rxn}^{vac} = E\left(C_3H_7O_3^*\right) + E\left(H^*\right) - E\left(C_3H_8O_3^*\right) - E\left(*\right) \qquad (1)$$

where $E\left(C_3H_7O_3^*\right)$, $E(H^*)$, and $E\left(C_3H_8O_3^*\right)$ are the electronic energies of $C_3H_7O_3^*$, H*, and glycerol $C_3H_8O_3^*$, and $E(*)$ is the electronic energy of the clean Pt(111) surface. The energies of the carbon-containing species can be obtained using DFT calculations or LSRs.

We define the reaction energy in the aqueous phase as being equal to the reaction energy in vacuum phase plus the change in the water–catalytic species interaction energy, as in our prior work,[34] *i.e.*,

$$E_{rxn}^{aq} = E_{rxn}^{vac} + \Delta E_{int} \qquad (2)$$

For any catalytic species, the water–catalytic species interaction energy E_{int} is defined as the total interaction between the water structure and the catalytic species.[33] For example, the interaction energy for glycerol is

$$E_{int}\left(C_3H_8O_3^*\right) = E\left(H_2O + C_3H_8O_3^*\right) - E\left(H_2O + *\right) - E\left(C_3H_8O_3^*\right) + E\left(*\right) \qquad (3)$$

E_{int} are reported as averages over 10 different configurations of water for catalytic species involved in non-water-mediated steps ± the calculated standard deviation. E_{int} for

This journal is © The Royal Society of Chemistry 2019

React. Chem. Eng., 2019, **4**, 383–392 | 385

catalytic species involved in water-mediated steps are calculated using a single configuration of H_2O molecules.

ΔE_{int} is the change in interaction energy going from reactants to products. For example, in the reaction $C_3H_8O_3^*$ dehydrogenation to $C_3H_7O_3^*$, ΔE_{int} is

$$\Delta E_{int} = E_{int}\left(C_3H_7O_3^*\right) + E_{int}\left(H^*\right) - E_{int}\left(C_3H_8O_3^*\right) - E_{int}\left(*\right) \quad (4)$$

We found that $E_{int}(H^*)$ is equal to 0. Further, $E_{int}(*)$, *i.e.*, E_{int} of the clean Pt(111) surface, is set to 0 by definition. Therefore, ΔE_{int} in this case can be calculated as $\Delta E_{int} = E_{int}\left(C_3H_7O_3^*\right) - E_{int}\left(C_3H_8O_3^*\right)$. When values of ΔE_{int} include ± values, they are the propagated uncertainties, which are determined using standard error propagation rules.[94]

Activation energies are calculated analogously. For example, the activation energy for the glycerol dehydrogenation reaction, $C_3H_8O_3^* + * \rightarrow TS^* + * \rightarrow C_3H_7O_3^* + H^*$ under vacuum is

$$E_{act}^{vac} = E\left(TS^*\right) - E\left(C_3H_8O_3^*\right) \quad (5)$$

where TS stands for transition state. Under aqueous phase, the activation energy is

$$E_{act}^{aq} = E_{act}^{vac} + \Delta E_{int} \quad (6)$$

where ΔE_{int} is the change of the interaction energy from the reactant to the transition state, *i.e.*,

$$\Delta E_{int} = E_{int}\left(TS^*\right) - E_{int}\left(C_3H_8O_3^*\right) \quad (7)$$

The above equations were used to calculate the activation energies in aqueous phase using DFT data. Since our TSS relationships are derived using transition states under aqueous phase, they already include the water–catalytic species interaction energy, and hence, the activation energy is simply

$$E_{act} = E(TS^*) - E(IS^*) \quad (8)$$

where IS stands for initial state and in this work is the reactant species.

2.6 Microkinetic modeling

Microkinetic modeling was performed with the MKMCXX package.[95] Adsorption rate constants were calculated from the Hertz–Knudsen equation,[96–98]

$$k_{ads} = \frac{yPA}{\sqrt{2\pi m k_B T}} \quad (9)$$

where y is the mole fraction of either the gas phase or aqueous phase species, P is the total pressure, A is the surface area of the adsorption site, m is molecular mass, k_B is the Boltzmann constant, and T is the temperature. Here, we set the initial mole fraction of glycerol to 0.1 for both the vacuum and aqueous phase microkinetic models. In the vacuum phase model, glycerol is supplied with a balance of inerts, and in the aqueous phase model, glycerol is supplied with a balance of H_2O (water : glycerol ratio of 9). The total pressure in both models is set to 1 atm. This procedure has been published previously by Heyden's group[51] for both gas and liquid phase microkinetic models. Essentially, it computes the adsorption rate constant from gas phase collision theory. To our knowledge, there is no well-tested theory for simulating the kinetics of chemisorption from liquid phase onto solid catalyst surfaces. Because of this, and also since our intent in this manuscript is to learn about the roles of H_2O molecules on surface reactions involved in the reforming of glycerol, we have treated the adsorption in our gas and aqueous phase models similarly. That said, we stress that there is some uncertainty embedded into the thermodynamic and kinetic quantities pertaining to adsorption that are reported in this manuscript.

Desorption rate constants were calculated as,[97–99]

$$k_{des} = \frac{k_B T^3}{h^3} \frac{A\left(2\pi m k_B\right)}{\sigma \theta_{rot}} \exp\left(\frac{-E_{des}}{k_B T}\right) \quad (10)$$

where h is the Plank's constant, σ is the symmetry number, θ is the rotational temperature of the species, and E_{des} is the desorption energy. Details about σ and θ are provided in the ESI† section S7. In this formalism, adsorption and desorption proceed through a mobile precursor, which is a fluid phase species that has been trapped on the catalyst surface. The mobile precursor has two translational degrees of freedom (while the fluid phase species has three) and three rotational degrees of freedom, which are all lost when the species ultimately binds to the catalyst surface. Desorption energies for all species considered in this work are endothermic (*i.e.*, their adsorption energies are exothermic).

Rate constants for surface reactions were calculated with the Arrhenius equation,

$$k = A\exp\left(\frac{-E_{act}}{k_B T}\right) \quad (11)$$

where A is the pre-exponential factor. Pre-exponential factors for surface reactions were set to 10^{13} s^{-1}.

Reaction energies and activation barriers that were input to the microkinetic model were obtained as follows. Energetics of reactions involving C3 species were calculated in this work using a combination of DFT data, LSRs, and TSS relationships, as described above. Modeling the APR of glycerol also requires energies of reactions involving C2 and C1 species and also water-gas shift. We obtained energies of these reactions from the literature, using references from Bligaard,[40] Heyden,[51] Vlachos,[52] and Schneider.[53] During the review stage of this manuscript, we became aware of a recently published database,[100] which houses structures and

386 | *React. Chem. Eng.*, 2019, **4**, 383–392

This journal is © The Royal Society of Chemistry 2019

energies of species involved in catalytic APR over Pt.[92] An alternative approach would have been to use information from the database for the reactions involving C2 and C1 species and water-gas shift. All reaction energetics that were used in the microkinetic models presented in this manuscript are tabulated in the ESI† section S7.

The microkinetic models reported in this work employed single site models for simplicity. We note that due to the large sizes of some of the adsorbates, as well as the fact that on supported catalysts, interfacial sites are likely important to the catalysis,[101] this is an approximation.

The temperature in our microkinetic models was set to 500 K. The MKM solver was iterated for 10^8 seconds to ensure convergence, and the absolute and relevant tolerances were both set to 10^{-8} mol s^{-1}.

3 Results

3.1 Role of H$_2$O on the energetics of reactions involving C$_3$H$_y$O$_3$ species

Reaction energies and activation barriers for non-water-mediated reactions are summarized in Table 1. Comparing the calculated reaction energies for vacuum and aqueous phases, the differences for the dehydrogenation steps are slight, indicating little influence of water. In contrast, reaction energies for decarbonylation steps are more endothermic in aqueous phase than in vacuum. Further, the energies of hydrogenolysis reactions 15, 16, and 18 are more exothermic in aqueous phase than in vacuum. To investigate the influence of water on the calculated activation barriers, Fig. 1 plots the activation energies for the three types of reactions in both vacuum and aqueous phases. As shown in Fig. 1a, the activation barriers for dehydrogenation reactions are for the most part similar in aqueous and vacuum phases. The activation barriers in the aqueous phase for decarbonylation reactions are larger than those under vacuum, with the exception of the activation barrier for Reaction 13 (CO–COH–COH* + * → COH–COH* + CO*), suggesting that there is a kinetic penalty for removing a carbonyl group from a C$_3$H$_y$O$_3$ catalytic intermediate under aqueous phase until a certain degree of dehydrogenation has occurred. Similarly, there is a kinetic penalty for removing a hydroxyl group from a C3 catalytic species under aqueous phase until a certain degree of dehydrogenation has occurred.

TSS relationships derived for non-water-mediated dehydrogenation, decarbonylation, and hydrogenolysis steps under vacuum and aqueous phases are shown in Fig. 2. Comparing the TSS relationships derived for vacuum phase to those derived for aqueous phase, the dehydrogenation trends are only minorly different, whereas the decarbonylation and hydrogenolysis trends are significantly different. This means that the E_{int} for the transition states involved in dehydrogenation reactions are similar to the E_{int} of the product species, whereas the E_{int} for the transition states involved in decarbonylation and hydrogenolysis reactions are different than the E_{int} of the product species for those reactions. Thus, water interacts with the reactants, transition states, and products involved in dehydrogenation of C3 species similarly, whereas water interacts with the reactants, transition states, and products involved in decarbonylation and hydrogenolysis of C3 species differently. Specifically, the water environment stabilizes the reactants and transition states of the decarbonylation reactions more so than the products, and the water environment stabilizes reactant and product species of hydrogenolysis reactions more so than the transition states.

3.2 Role of H$_2$O on the mechanisms of reactions involving C$_3$H$_y$O$_3$ species

Mechanistically, H$_2$O molecules can mediate catalytic dehydrogenation reactions, forming H$_{2n+1}$O$_n$ complexes at either the transition state or as the product,[27,102–109] and H$_{2n+1}$O$_n$

Table 1 Reaction energies (E_{rxn}) and activation energies (E_{act}) of non-water-mediated dehydrogenation (1–7), decarbonylation (8–13), and hydrogenolysis steps (14–18) under vacuum (vac) and aqueous phases (aq). Reaction numbers of the analogous water-mediated reactions are given in parentheses where applicable, the results for which are given in Table 2. All values are in units of eV

| Number	Reaction	E_{rxn}^{vac}	E_{rxn}^{aq}	E_{act}^{vac}	E_{act}^{aq}
1	CH$_2$OH–CHOH–CH$_2$OH* + * → CH$_2$OH–COH–CH$_2$OH* + H*	−0.45	−0.44 ± 0.10	0.36	0.30 ± 0.10
2 (19)	CH$_2$OH–COH–CH$_2$OH* + * → CHOH–COH–CH$_2$OH* + H*	−0.35	−0.39 ± 0.14	0.60	0.48 ± 0.11
3 (20)	CHOH–COH–CH$_2$OH* + * → CHOH–COH–CHOH* + H*	−0.08	−0.10 ± 0.10	1.01	1.09 ± 0.10
4 (21)	CHOH–COH–CHOH* + * → COH–COH–CHOH* + H*	−0.19	−0.11 ± 0.11	0.38	0.35 ± 0.14
5 (22)	COH–COH–CHOH* + * → COH–COH–COH* + H*	−0.33	−0.38 ± 0.12	0.47	0.45 ± 0.14
6 (23)	COH–COH–COH* + * → CO–COH–COH* + H*	0.20	0.24 ± 0.10	0.40	0.38 ± 0.12
7 (24)	CO–COH–COH* + * → CO–COH–CO* + H*	0.26	0.26 ± 0.09	0.67	0.66 ± 0.08
8	CO–CHOH–CH$_2$OH* + * → CHOH–CH$_2$OH* + CO*	−0.94	−0.52 ± 0.17	1.08	0.90 ± 0.18
9	CO–COH–CH$_2$OH* + * → COH–CH$_2$OH* + CO*	−0.61	−0.34 ± 0.16	0.30	0.43 ± 0.10
10	CO–CHOH–CHOH* + * → CHOH–CHOH* + CO*	−1.17	−1.03 ± 0.14	0.56	0.60 ± 0.14
11	CO–COH–CHOH* + * → COH–CHOH* + CO*	−0.61	−0.55 ± 0.10	0.46	0.72 ± 0.12
12	CO–CHOH–COH* + * → CHOH–COH* + CO*	−0.34	0.15 ± 0.12	0.37	0.70 ± 0.15
13	CO–COH–COH* + * → COH–COH* + CO*	−0.96	−0.81 ± 0.13	0.14	0.01 ± 0.16
14 (25)	COH–CHOH–CH$_2$OH* + * → C–CHOH–CH$_2$OH* + OH*	0.30	0.37 ± 0.10	0.96	1.12 ± 0.12
15 (26)	CHOH–COH–CHOH* + * → CHOH–C–CHOH* + OH*	0.68	0.49 ± 0.14	1.55	1.65 ± 0.18
16 (27)	COH–COH–CHOH* + * → C–COH–CHOH* + OH*	0.40	0.20 ± 0.13	1.05	0.94 ± 0.12
17 (28)	COH–CO–CH$_2$OH* + * → C–CO–CH$_2$OH* + OH*	0.72	0.81 ± 0.11	0.93	0.99 ± 0.16
18 (29)	COH–COH–COH* + * → C–COH–COH* + OH*	2.53	2.07 ± 0.15	2.92	2.43 ± 0.13
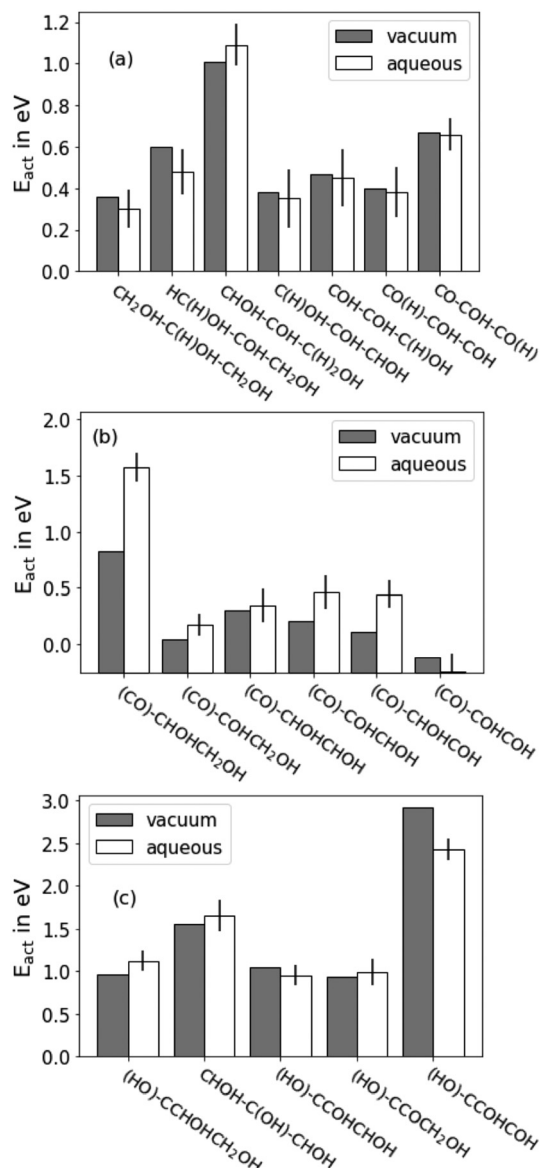
Fig. 1 Comparison of activation energies calculated in vacuum (gray) and aqueous phases (white) for the non-water-mediated dehydrogenation (a), decarbonylation (b), and hydrogenolysis steps (c) calculated in this work. Bar labels are the transition state species with the species that is being removed in parentheses. Error bars denote the propagated uncertainties of the average energies (caused by configurational fluctuations of the liquid H_2O molecules).
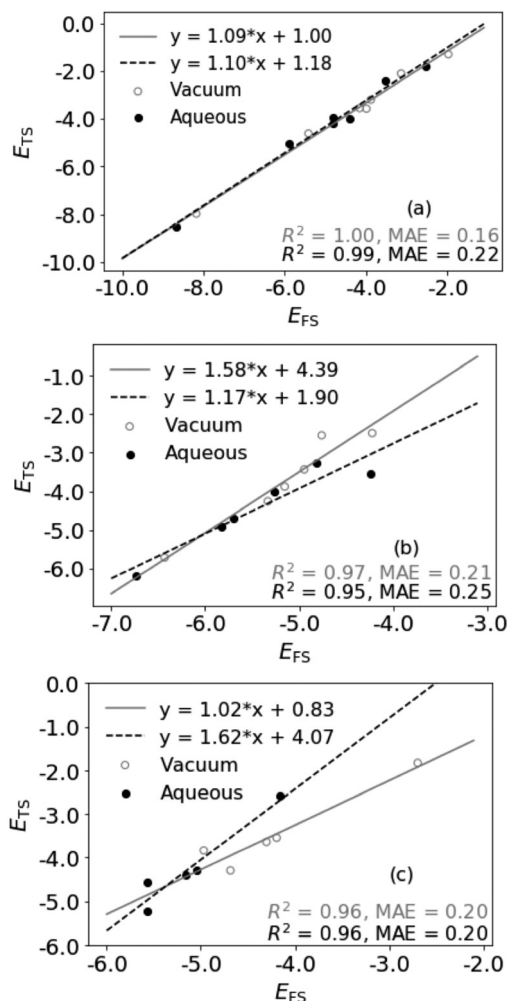

Fig. 2 Regression training data (points) and linear TSS relationships (lines) for non-water-mediated dehydrogenation (a), decarbonylation (b), and hydrogenolysis steps (c) calculated under vacuum (solid lines and unfilled points) and aqueous phases (dotted lines and filled points). MAE stands for mean absolute error. Units on all values are eV.

complexes can act as reactants in hydrogenolysis steps.[110] We calculated the energetics of 15 such water-mediated reactions, and they are presented in Table 2. The reaction energies for the water-mediated C–H dehydrogenation steps are in general more endothermic than their non-water-mediated analogues, whereas the reaction energies for water-mediated O–H dehydrogenation steps are more exothermic than their non-water-mediated analogues, going from being endothermic to exothermic in both cases that we explicitly calculated (reactions 23 and 24, i.e., COH–COH–COH* + H_2O^* → CO–COH–COH* + H_3O^* and CO–COH–COH* + H_2O^* → CO–

COH–CO* + H_3O^*). The reaction energies for water-mediated hydrogenolysis steps are for the most part similar to their non-water-mediated analogues, with the exception of reaction 27 (COH–COH–CHOH* + H_2O^* → C–COH–CHOH* + H_3O^*), which is 0.18 eV more exothermic.

Activation energies for water-mediated versus non-water-mediated reactions are shown in Fig. 3. The activation energies for the water-mediated C–H scissions are all larger than their non-water-mediated analogues. In fact, with the exception of reaction 22, the activation barriers for the water-mediated C–H scissions are all greater than 1 eV. The barrier for reaction 22, i.e., COH–COH–CHOH* reacting to COH–COH–COH*, is 0.57 eV, compared to 0.45 eV for its non-water-mediated analogue. The barriers for water-mediated O–H scissions (reactions 23 and 24) are essentially equal to 0, which is lower than their non-water-mediated analogues. Barriers ≈0 are expected for proton transfer reactions in liquid H_2O.[111] The activation energies for water-mediated

Table 2 Reaction energies (E_{rxn}) and activation energies (E_{act}) of water-mediated dehydrogenation (19–25) and hydrogenolysis steps (25–29). Reaction energetics were calculated using one and/or two water molecules in the reactants. Numbers in parentheses are for the non-mediated analogues from Table 1. All values are in units of eV

Number	Reaction	E_{rxn}	E_{act}
19 (2)	$CH_2OH–COH–CH_2OH^* + H_2O^* \rightarrow CHOH–COH–CH_2OH^* + H_3O^*$	0.25	1.42
19 (2)	$CH_2OH–COH–CH_2OH^* + 2H_2O^* \rightarrow CHOH–COH–CH_2OH^* + H_5O_2^* + *$	0.26	1.18
20 (3)	$CHOH–COH–CH_2OH^* + H_2O^* \rightarrow CHOH–COH–CHOH^* + H_3O^*$	0.27	1.67
20 (3)	$CHOH–COH–CH_2OH^* + 2H_2O^* \rightarrow CHOH–COH–CHOH^* + H_5O_2^* + *$	0.26	1.75
21 (4)	$CHOH–COH–CHOH^* + H_2O^* \rightarrow COH–COH–CHOH^* + H_3O^*$	0.29	1.14
21 (4)	$CHOH–COH–CHOH^* + 2H_2O^* \rightarrow COH–COH–CHOH^* + H_5O_2^* + *$	0.37	1.20
22 (5)	$COH–COH–CHOH^* + H_2O^* \rightarrow COH–COH–COH^* + H_3O^*$	0.07	0.87
22 (5)	$COH–COH–CHOH^* + 2H_2O^* \rightarrow COH–COH–COH^* + H_5O_2^* + *$	−0.15	0.57
23 (6)	$COH–COH–COH^* + 2H_2O^* \rightarrow CO–COH–COH^* + H_5O_2^* + *$	−0.39	0.01
24 (7)	$CO–COH–COH^* + 2H_2O^* \rightarrow CO–COH–CO^* + H_5O_2^* + *$	−0.19	0.02
25 (14)	$COH–CHOH–CH_2OH^* + H_3O^* + * \rightarrow C–CHOH–CH_2OH^* + 2H_2O^*$	0.30	0.23
26 (15)	$CHOH–COH–CHOH^* + H_3O^* + * \rightarrow CHOH–C–CHOH^* + 2H_2O^*$	0.62	0.64
27 (16)	$COH–COH–CHOH^* + H_3O^* + * \rightarrow C–COH–CHOH^* + 2H_2O^*$	0.38	0.31
28 (17)	$COH–CO–CH_2OH^* + H_3O^* + * \rightarrow C–CO–CH_2OH^* + 2H_2O^*$	0.70	0.28
29 (18)	$COH–COH–COH^* + H_3O^* + * \rightarrow C–COH–COH^* + 2H_2O^*$	2.03	1.51

hydrogenolysis reactions are lower than their non-mediated analogues, suggesting that hydrogenolysis steps could occur *via* water mediated routes, if sufficient concentration of $H_{2n+1}O_n$ species were available.

3.3 Microkinetic modeling results

The reaction energetics calculated in this work, along with the TSS relationships that were derived, as well as reaction energetics available in the literature[40,51–53] allow for microkinetic modeling of catalytic glycerol reforming. We ran microkinetic models under both vacuum and aqueous phases. In vacuum phase, the initial water concentration was set to 0, so the water-gas shift reaction did not occur. Hence,
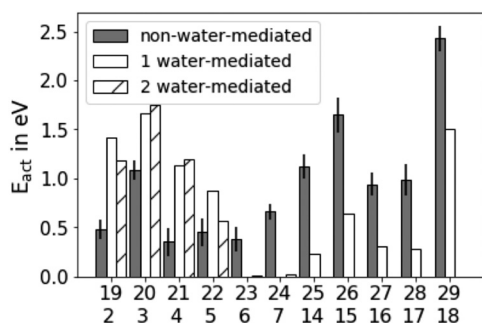

Fig. 3 Comparison of activation energies for non-water-mediated (gray bars) reactions to their water-mediated (white and hashed bars) analogues. White bars indicate participation of $1H_2O$ molecule, and hashed bars indicate participation of $2H_2O$ molecules. Sets of bars are labeled by their reaction numbers. The first row of numbers are the reaction numbers for the water-mediated reactions (from Table 2), and the second row of numbers are the reaction numbers for their non-water-mediated analogues (from Table 1).

the main products were H_2 and CO. In aqueous phase, the water supplied OH^* to the surface, which reacted with CO^* through water-gas shift steps.[53] The primary products in the aqueous phase model were H_2, CO_2, and $CH_2OH–CH_2OH$ (ethylene glycol). Assuming the gas phase products are H_2 and CO_2, the mole fraction of H_2 in the gas phase was 65.6%, which agrees well with the experimental value of 64.8% observed by Cortright *et al.*[3] Further, the selectivity to H_2 was 89.1%, compared to the experimental value of 85.0% reported by Lehnert *et al.*[112] 32.8% of the carbon was converted to CO_2, in agreement with the experimentally observed value of 29.7% reported by Cortright *et al.*[3]

Reactions that contributed to the observed phenomena in both models along with their net rates are tabulated in ESI† section S8. Under vacuum, glycerol decomposition proceeds through dehydrogenation steps until reaching the CO–COH–COH* intermediate, which then proceeds through a decarbonylation step to form COH–COH*. This intermediate is then further dehydrogenated to CO–CO*, which is finally decomposed into 2CO*. The pathway in aqueous phase is similar, with dehydrogenation occurring until reaching the CO–COH–COH* intermediate. However, water-mediated reactions become competitive with non-water-mediated reactions for both O–H and C–H scissions. Specifically, the rates of water-mediated COH–COH–CHOH* dehydrogenation to COH–COH–COH*, COH–COH–COH* dehydrogenation to CO–COH–COH*, and CO–COH–COH* dehydrogenation to CO–COH–CO* reactions are competitive with their non-water-mediate analogues. The CO–COH–COH* intermediate that is formed from water-mediated COH–COH–COH* dehydrogenation is decarbonylated to COH–COH*, which is dehydrogenated to CO–CO* and then decomposed to 2CO*, like under vacuum. Similarly, the CO–COH–CO* that is formed from

This journal is © The Royal Society of Chemistry 2019

React. Chem. Eng., 2019, **4**, 383–392 | 389

water-mediated CO–COH–COH* dehydrogenation is dehydrogenated to CO–CO–CO* and then decomposed into 3CO*. In both microkinetic models, carbon atoms must be significantly dehydrogenated before the rates of O–H scissions start to become appreciable. Hydrogenolysis steps do not participate in the dominant reaction pathways for either the vacuum or aqueous-phase models. However, we note that our microkinetic model of the aqueous phase reforming of glycerol was carried out at neutral pH, which resulted in insufficient concentration of $H_{2n+1}O_n$ species to carry out water-mediated hydrogenolysis to any remarkable degree, despite that the rate constants for these reactions are larger than the non-water-mediated analogues.

4 Discussion

From the results of the last section, H_2O plays at least four roles in the aqueous phase reforming of glycerol. One, H_2O molecules dissociate on the catalyst surface, supplying the OH* and H* that are needed to promote oxidation of CO* and production of H_2. Two, H_2O molecules promote C–H scission. We find that the activation barrier for water-mediated COH–COH–CHOH* dehydrogenation to COH–COH–COH* is within 0.12 eV (although still higher) of its non-water-mediated analogue. The reaction energy of the water-mediated reaction is less exothermic than its non-water-mediated analogue by more than 0.2 eV; however, owing to the large concentration of H_2O, the rate of the water-mediated COH–COH–CHOH* dehydrogenation to COH–COH–COH* is competitive with its non-water-mediated analogue. Three, water molecules mediate O–H scission. The activation barriers of H_2O-mediated O–H scissions are ≈0 and their reaction energies are exothermic. Thus the rates of water-mediated O–H scissions are higher than their non-water-mediated analogues, by up to five orders of magnitude. Four, water inhibits the thermodynamics of catalytic decarbonylation. Specifically, in both microkinetic models, decarbonylation occurs at the CO–COH–COH* species. The activation energy for the decarbonylation step to COH–COH* is quite low in both vacuum and aqueous phases (0.14 eV in vacuum versus 0.01 eV in aqueous phase); however, the reaction energy is 0.17 eV more endothermic in aqueous phase than it is in vacuum. This is due to the loss of hydrophilicity that occurs over the course of the reaction. Specifically, E_{int} for CO–COH–COH* is more negative than for the combination of COH–COH* and CO* (with E_{int} for CO* being essentially equal to zero[33]). In fact, comparing the reaction energies in vacuum versus aqueous phase for all of the decarbonylation reactions calculated in this work, there is always an energy penalty associated, ranging from 0.06 eV (CO–COH–CHOH* → COH–CHOH*) to 0.49 eV (CO–CHOH–COH* → CHOH–COH*).

5 Conclusions

In this work, we have used DFT calculations, MD simulations, linear scaling relationships, transition state scaling relationships, and data from the literature to construct micro-kinetic models of catalytic glycerol reforming under vacuum and aqueous phases. We have specifically calculated steps in the pathways for dehydrogenation, decarbonylation, and hydrogenolysis of C3 species, and we have included steps where H_2O molecules and $H_{(2n+1)}O_n$ species explicitly participate in the reactions. Results from our microkinetic models identified four roles of water on the catalytic mechanism of aqueous phase reforming of glycerol: supplying OH* needed in water-gas shift to oxidize CO*, promoting C–H scissions, promoting O–H scissions, and thermodynamically inhibiting decarbonylation of C3 species. Our results also suggest that protons in solution could mediate catalytic hydrogenolysis reactions if the reaction were run under sufficient pH (in practice, hydrogenolysis reactions are likely promoted by acid sites on the catalyst or its support[113]). In this manuscript, we have attempted to present only the "big-picture" conclusions. This is because, even with the inclusion of an explicit liquid water environment and an extensive network of catalytic reactions, limitations in our models prevent us from providing a comprehensive mechanism of glycerol APR. For example, methods to properly model adsorption and desorption at a liquid water/catalyst interface and models that properly incorporate the participation of interfacial sites are needed to more fully understand the mechanism of glycerol APR. We are presently working on addressing both issues.

Conflicts of interest

There are no conflicts to declare.

Acknowledgements

References

1 G. W. Huber, R. D. Cortright and J. A. Dumesic, *Angew. Chem.*, 2004, **116**, 1575–1577.

2 G. W. Huber, J. N. Chheda, C. J. Barrett and J. A. Dumesic, *Science*, 2005, **308**, 1446–1450.

3 R. D. Cortright, R. R. Davda and J. A. Dumesic, *Nature*, 2002, **418**, 964–967.

4 J. C. Serrano-Ruiz, R. Luque and A. Sepúlveda-Escribano, *Chem. Soc. Rev.*, 2011, **40**, 5266–5281.

5 Q. Bu, H. Lei, A. H. Zacher, L. Wang, S. Ren, J. Liang, Y. Wei, Y. Liu, J. Tang and Q. Zhang, *et al.*, *Bioresour. Technol.*, 2012, **124**, 470–477.

6 Y. Chen, M. Salciccioli and D. G. Vlachos, *J. Phys. Chem. C*, 2011, **115**, 18707–18720.

390 | *React. Chem. Eng.*, 2019, **4**, 383–392

This journal is © The Royal Society of Chemistry 2019

7 M. Salciccioli, W. Yu, M. A. Barteau, J. G. Chen and D. G. Vlachos, *J. Am. Chem. Soc.*, 2011, **133**, 7996–8004.

8 V. Vorotnikov, G. Mpourmpakis and D. G. Vlachos, *ACS Catal.*, 2012, **2**, 2496–2504.

9 R. S. Assary and L. A. Curtiss, *Energy Fuels*, 2012, **26**, 1344–1352.

10 J. Lu, S. Behtash and A. Heyden, *J. Phys. Chem. C*, 2012, **116**, 14328–14341.

11 B. Liu and J. Greeley, *Phys. Chem. Chem. Phys.*, 2013, **15**, 6475.

12 J. Lu, S. Behtash, O. Mamun and A. Heyden, *ACS Catal.*, 2015, **5**, 2423–2435.

13 Y. Okamoto, O. Sugino, Y. Mochizuki, T. Ikeshoji and Y. Morikawa, *Chem. Phys. Lett.*, 2003, **377**, 236–242.

14 C. Hartnig and E. Spohr, *Chem. Phys.*, 2005, **319**, 185–191.

15 C. Hartnig, J. Grimminger and E. Spohr, *J. Electroanal. Chem.*, 2007, **607**, 133–139.

16 C. Hartnig, J. Grimminger and E. Spohr, *Electrochim. Acta*, 2007, **52**, 2236–2243.

17 J. A. Santana, C. R. Cabrera and Y. Ishikawa, *Phys. Chem. Chem. Phys.*, 2010, **12**, 9526.

18 N. Artrith and A. M. Kolpak, *Nano Lett.*, 2014, **14**, 2670–2676.

19 R. Jinnouchi, K. Kodama and Y. Morimoto, *J. Electroanal. Chem.*, 2014, **716**, 31–44.

20 J. Liu, X.-M. Cao and P. Hu, *Phys. Chem. Chem. Phys.*, 2014, **16**, 4176.

21 Y. Yoon, R. Rousseau, R. S. Weber, D. Mei and J. A. Lercher, *J. Am. Chem. Soc.*, 2014, **136**, 10287–10298.

22 J. K. Nørskov, J. Rossmeisl, A. Logadottir, L. Lindqvist, J. R. Kitchin, T. Bligaard and H. Jónsson, *J. Phys. Chem. B*, 2004, **108**, 17886–17892.

23 S. Behtash, J. Lu, M. Faheem and A. Heyden, *Green Chem.*, 2014, **16**, 605–616.

24 S. Behtash, J. Lu, M. Faheem and A. Heyden, *Green Chem.*, 2014, **16**, 605–616.

25 S. Behtash, J. Lu and A. Heyden, *Catal. Sci. Technol.*, 2014, **4**, 3981–3992.

26 M. Saleheen and A. Heyden, *ACS Catal.*, 2018, **8**, 2188–2194.

27 X. Nie, W. Luo, M. J. Janik and A. Asthagiri, *J. Catal.*, 2014, **312**, 108–122.

28 Y. Gohda, S. Schnur and A. Groß, *Faraday Discuss.*, 2009, **140**, 233–244.

29 A. Pavlova and E. J. Meijer, *ChemPhysChem*, 2012, **13**, 3492–3496.

30 C. Michel, F. Auneau, F. Delbecq and P. Sautet, *ACS Catal.*, 2011, **1**, 1430–1440.

31 C. Michel, J. Zaffran, A. M. Ruppert, J. Matras-Michalska, M. Jędrzejczyk, J. Grams and P. Sautet, *Chem. Commun.*, 2014, **50**, 12450–12453.

32 J. Saavedra, H. A. Doan, C. J. Pursell, L. C. Grabow and B. D. Chandler, *Science*, 2014, **345**, 1599–1602.

33 C. J. Bodenschatz, S. Sarupria and R. B. Getman, *J. Phys. Chem. C*, 2015, **120**, 801.

34 T. Xie, S. Sarupria and R. B. Getman, *Mol. Simul.*, 2017, **43**, 370–378.

35 F. Abild-Pedersen, J. Greeley, F. Studt, J. Rossmeisl, T. R. Munter, P. G. Moses, E. Skúlason, T. Bligaard and J. K. Nørskov, *Phys. Rev. Lett.*, 2007, **99**, 016105.

36 J. Gómez-Díaz, C. Vargas-Fuentes and N. López, *J. Chem. Phys.*, 2011, **135**, 124707.

37 J. Gómez-Díaz and N. López, *J. Phys. Chem. C*, 2011, **115**, 5667–5674.

38 G. Jones, T. Bligaard, F. Abild-Pedersen and J. K. Nørskov, *J. Phys.: Condens. Matter*, 2008, **20**, 064239.

39 I. C. Man, H.-Y. Su, F. Calle-Vallejo, H. A. Hansen, J. I. Martínez, N. G. Inoglu, J. Kitchin, T. F. Jaramillo, J. K. Nørskov and J. Rossmeisl, *ChemCatChem*, 2011, **3**, 1159–1165.

40 S. Wang, V. Petzold, V. Tripkovic, J. Kleis, J. G. Howalt, E. Skúlason, E. M. Fernández, B. Hvolbæk, G. Jones, A. Toftelund, H. Falsig, M. Björketun, F. Studt, F. Abild-Pedersen, J. Rossmeisl, J. K. Nørskov and T. Bligaard, *Phys. Chem. Chem. Phys.*, 2011, **13**, 20760.

41 A. Asthagiri and M. J. Janik, *Computational catalysis*, Royal Society of Chemistry, 2013, pp. 1–58.

42 *Computational Catalysis*, ed. A. Asthagiri and M. J. Janik, The Royal Society of Chemistry, 2014, pp. P001–266.

43 J. Greeley, *Annu. Rev. Chem. Biomol. Eng.*, 2016, **7**, 605–635.

44 J. Nørskov, T. Bligaard, A. Logadottir, S. Bahn, L. Hansen, M. Bollinger, H. Bengaard, B. Hammer, Z. Sljivancanin, M. Mavrikakis, Y. Xu, S. Dahl and C. Jacobsen, *J. Catal.*, 2002, **209**, 275–278.

45 P. Ferrin, D. Simonetti, S. Kandoi, E. Kunkes, J. A. Dumesic, J. K. Nørskov and M. Mavrikakis, *J. Am. Chem. Soc.*, 2009, **131**, 5809–5815.

46 B. Liu and J. Greeley, *J. Phys. Chem. C*, 2011, **115**, 19702–19709.

47 B. Liu, L. Cheng, L. Curtiss and J. Greeley, *Surf. Sci.*, 2014, **622**, 51–59.

48 B. Liu, M. Zhou, M. K. Y. Chan and J. P. Greeley, *ACS Catal.*, 2015, **5**, 4942–4950.

49 R. Alcala, *J. Catal.*, 2003, **218**, 178–190.

50 D. Loffreda, F. Delbecq, F. Vigné and P. Sautet, *Angew. Chem.*, 2009, **121**, 9140–9142.

51 M. Faheem, M. Saleheen, J. Lu and A. Heyden, *Catal. Sci. Technol.*, 2016, **6**, 8242–8256.

52 Y. Chen and D. G. Vlachos, *J. Phys. Chem. C*, 2010, **114**, 4973–4982.

53 J. P. Clay, J. P. Greeley, F. H. Ribeiro, W. N. Delgass and W. F. Schneider, *J. Catal.*, 2014, **320**, 106–117.

54 L. Bellarosa, R. García-Muelas, G. Revilla-López and N. López, *ACS Cent. Sci.*, 2016, **2**, 109–116.

55 C. J. Bodenschatz, X. Zhang, T. Xie, S. Sarupria and R. B. Getman, *J. Visualized Exp.*, 2018, submitted.

56 C. Vega, J. Abascal and I. Nezbeda, *J. Chem. Phys.*, 2006, **125**, 034503.

57 J. Brodholt and B. Wood, *J. Geophys. Res.: Solid Earth*, 1993, **98**, 519–536.

58 K. Yoshida, C. Wakai, N. Matubayasi and M. Nakahara, *J. Chem. Phys.*, 2005, **123**, 164506.

59 S. Plimpton, *J. Comput. Phys.*, 1995, **117**, 1–19.

This journal is © The Royal Society of Chemistry 2019

React. Chem. Eng., 2019, **4**, 383–392 | 391

60 W. L. Jorgensen and J. Tirado-Rives, *J. Am. Chem. Soc.*, 1988, **110**, 1657–1666.

61 J. L. Abascal and C. Vega, *J. Chem. Phys.*, 2005, **123**, 234505.

62 H. Heinz, T.-J. Lin, R. K. Mishra and F. S. Emami, *Langmuir*, 2013, **29**, 1754–1765.

63 H. A. Lorentz, *Ann. Phys.*, 1881, **248**, 660–661.

64 M. Schoen and C. Hoheisel, *Mol. Phys.*, 1984, **52**, 1029–1042.

65 T. A. Manz and D. S. Sholl, *J. Chem. Theory Comput.*, 2010, **6**, 2455–2468.

66 T. A. Manz and D. S. Sholl, *J. Chem. Theory Comput.*, 2011, **7**, 4146–4164.

67 T. A. Manz and D. S. Sholl, *J. Chem. Theory Comput.*, 2012, **8**, 2844–2867.

68 T. A. Manz and N. G. Limas, *RSC Adv.*, 2016, **6**, 47771–47801.

69 N. G. Limas and T. A. Manz, *RSC Adv.*, 2016, **6**, 45727–45747.

70 T. A. Manz, *RSC Adv.*, 2017, **7**, 45552–45581.

71 G. Wen, Y. Xu, H. Ma, Z. Xu and Z. Tian, *Int. J. Hydrogen Energy*, 2008, **33**, 6657–6666.

72 D. D. Hibbitts, B. T. Loveless, M. Neurock and E. Iglesia, *Angew. Chem.*, 2013, **125**, 12499–12504.

73 D. L. King, L. Zhang, G. Xia, A. M. Karim, D. J. Heldebrant, X. Wang, T. Peterson and Y. Wang, *Appl. Catal., B*, 2010, **99**, 206–213.

74 Y. Xu, Z. Tian, G. Wen, Z. Xu, W. Qu and L. Lin, *Chem. Lett.*, 2006, **35**, 216–217.

75 G. J. Martyna, M. L. Klein and M. Tuckerman, *J. Chem. Phys.*, 1992, **97**, 2635–2643.

76 G. Kresse and J. Hafner, *Phys. Rev. B: Condens. Matter Mater. Phys.*, 1993, **48**, 13115–13118.

77 G. Kresse, *J. Non-Cryst. Solids*, 1995, **192–193**, 222–229.

78 G. Kresse and J. Furthmüller, *Comput. Mater. Sci.*, 1996, **6**, 15–50.

79 G. Kresse and J. Furthmüller, *Phys. Rev. B: Condens. Matter Mater. Phys.*, 1996, **54**, 11169–11186.

80 G. Kresse and J. Hafner, *Phys. Rev. B: Condens. Matter Mater. Phys.*, 1993, **48**, 13115–13118.

81 G. Kresse and D. Joubert, *Phys. Rev. B: Condens. Matter Mater. Phys.*, 1999, **59**, 1758–1775.

82 J. P. Perdew, K. Burke and M. Ernzerhof, *Phys. Rev. Lett.*, 1996, **77**, 3865–3868.

83 S. Grimme, *J. Comput. Chem.*, 2006, **27**, 1787–1799.

84 M. Korth, *Org. Biomol. Chem.*, 2013, **11**, 6515–6519.

85 W. Liu, V. G. Ruiz, G.-X. Zhang, B. Santra, X. Ren, M. Scheffler and A. Tkatchenko, *New J. Phys.*, 2013, **15**, 053046.

86 N. Almora-Barrios, G. Carchini, P. Błoński and N. López, *J. Chem. Theory Comput.*, 2014, **10**, 5002–5009.

87 J. D. Pack and H. J. Monkhorst, *Phys. Rev. B: Solid State*, 1976, **13**, 5188.

88 G. Henkelman and H. Jónsson, *J. Chem. Phys.*, 2000, **113**, 9978–9985.

89 G. Henkelman, B. P. Uberuaga and H. Jónsson, *J. Chem. Phys.*, 2000, **113**, 9901–9904.

90 G. Henkelman and H. Jónsson, *J. Chem. Phys.*, 1999, **111**, 7010–7022.

91 https://github.com/getman-research-group/Geomtry-files-for-Insights-into-the-Roles-of-Water-on-the-Aqueous-Phase-Reforming-of-Glycerol, (accessed Dec, 2018).

92 Q. Li, R. García-Muelas and N. López, *Nat. Commun.*, 2018, **9**, 526.

93 R. García-Muelas, M. Rellán-Piñeiro, Q. Li and N. López, *ChemCatChem*, 2018, DOI: 10.1002/cctc.201801271.

94 P. R. Bevington, D. K. Robinson, J. M. Blair, A. J. Mallinckrodt and S. McKay, *Comput. Phys.*, 1993, **7**, 415–416.

95 I. A. W. Filot, R. A. van Santen and E. J. M. Hensen, *Angew. Chem., Int. Ed.*, 2014, **53**, 12746–12750.

96 K. W. Kolasinski, *Surface science: foundations of catalysis and nanoscience*, John Wiley & Sons, 2012, p. 203.

97 I. A. Filot, R. J. Broos, J. P. van Rijn, G. J. van Heugten, R. A. van Santen and E. J. Hensen, *ACS Catal.*, 2015, **5**, 5453–5467.

98 I. A. Filot, B. Zijlstra, R. J. Broos, W. Chen, R. Pestman and E. J. Hensen, *Faraday Discuss.*, 2017, **197**, 153–164.

99 A. P. J. Jansen, *Modeling Surface Reactions I*, Springer Berlin Heidelberg, Berlin, Heidelberg, 2012, pp. 121–153.

100 M. Álvarez-Moreno, C. De Graaf, N. Lopez, F. Maseras, J. M. Poblet and C. Bo, *J. Chem. Inf. Model.*, 2014, **55**, 95–103.

101 M. Cargnello, V. V. Doan-Nguyen, T. R. Gordon, R. E. Diaz, E. A. Stach, R. J. Gorte, P. Fornasiero and C. B. Murray, *Science*, 2013, **341**, 771–773.

102 M. Neurock, S. A. Wasileski and D. Mei, *Chem. Eng. Sci.*, 2004, **59**, 4703–4714.

103 X. Nie, M. R. Esopi, M. J. Janik and A. Asthagiri, *Angew. Chem., Int. Ed.*, 2013, **125**, 2519–2522.

104 Y. Zhao and T. Gennett, *Phys. Rev. Lett.*, 2014, **112**, 076101.

105 T. Cheng, H. Xiao and W. A. Goddard, *J. Am. Chem. Soc.*, 2016, **138**, 13802–13805.

106 T. Loerting and K. R. Liedl, *J. Phys. Chem. A*, 2001, **105**, 5137–5145.

107 C. Hartnig and E. Spohr, *Chem. Phys.*, 2005, **319**, 185–191.

108 S. Dong, W. Shi, J. Zhang and S. Bi, *ACS Earth Space Chem.*, 2018, **2**, 269–277.

109 L. Árnadóttir, E. M. Stuve and H. Jónsson, *Chem. Phys. Lett.*, 2012, **541**, 32–38.

110 N. Spang, M. Müller and M. R. Buchner, *Eur. J. Inorg. Chem.*, 2018, **2018**, 3652–3659.

111 D. Marx, *ChemPhysChem*, 2006, **7**, 1848–1870.

112 K. Lehnert and P. Claus, *Catal. Commun.*, 2008, **9**, 2543–2546.

113 A. Martin, U. Armbruster, I. Gandarias and P. L. Arias, *Eur. J. Lipid Sci. Technol.*, 2013, **115**, 9–27.

392 | *React. Chem. Eng.*, 2019, **4**, 383–392

This journal is © The Royal Society of Chemistry 2019